Wideband 2 × 2 antenna-in-package based on magneto-electric dipole array antenna for 5G mmWave applications

Wai Yan Yong[1,2] and Andrés Alayón Glazunov[1,3]*

[1]Department of Electrical Engineering, University of Twente, Enschede, Netherlands, [2]Rohde & Schwarz GmbH Co. KG, Munich, Germany, [3]Department of Science and Technology, Linköping University, Linköping, Sweden

This paper presents an antenna-in-package (AiP) design realised with the conventional multi-layer printed circuit board manufacturing method. The design consists of a wideband 2 × 2 magneto-electric dipole array antenna operating from 24.25 – 29.5 GHz and a wideband transition from the analogue beamformer integrated into the proposed MED array antenna (IMED). The IMED array antenna has been fabricated with two distinct NXP analogue beamformer chips, i.e., *MMW 9004 KC* and *MMW 9002 KC* covering the N257 and the N258 band, respectively. The measured effective isotropic radiated power at P1dB was 35.3 dBm and 35.1 dBm for the IMED with the *MMW 9004 KC* and the *MMW 9002 KC* analogue beamformer chip, respectively. Our proposed antenna demonstrates the feasibility of designing a single wideband AiP that can be integrated with different analogue beamformers operating within the frequency band of the proposed antenna. This is true, provided the RFIC used for integration has the same footprint for RF ports, serial peripheral interface control ports, and DC power supply ports. The primary benefit of the proposed technique is the design antenna can adapt the operating frequency to different frequency standards by incorporating additional analogue chips without increasing the design complexity. This feature enables the antenna manufacturer to tailor the antenna products to different frequency standardisations depending on where the antenna will be employed. The AiP operates at 5G millimeter-wave (mmWave) frequencies, with the potential for Internet of Things applications. Furthermore, from our simulation results, the proposed IMED can potentially be extended as a phased array antenna with 2D scanning.

KEYWORDS

antenna-in-package (AiP), fifth generation (5G), millimeter-wave (mmwave), ME-dipole, phased array antenna

1 Introduction

With the advancements in wireless communications and smart device technologies, the Internet of Things (IoTs) has increased with ubiquitous sensing and computing capabilities to connect millions of devices over the internet Mehmood et al. (2017); Aoudia et al., 2024 With the enormous advantages offered by IoT, great attention has

been directed towards massive industrial applications such as smart manufacturing Wollschlaeger et al. (2017); Liao et al. (2018), IoT for medical monitoring Kumar and Chand (2020); Da Costa Nascimento et al., 2024, and autonomous driving Minovski et al. (2020). Nonetheless, these IoT applications necessitate using far more sophisticated communication technologies with low latency and ultra-reliable communication networks. Therefore, it is expected that 5G communication will serve as the backbone for the next-generation of wireless devices. 5G wireless communications are anticipated to simultaneously provide peak data rates of up to 10 Gbps to multiple users with low latency ETSI (2013); GSMA Intelligence (2021); Mehmood et al. (2017). The millimetre-wave (mmWave) band has received great interest in achieving this ambitious objective Alibakhshikenari et al., 2021a, Alibakhshikenari et al., 2021b It provides large chunks of wideband spectrum, enabling higher data throughput than in existing networks operating below 6 GHz GSMA Intelligence (2021); Mehmood et al. (2017). However, mmWave signals suffer from increased propagation losses, which can be mitigated by employing array antennas and beamforming technologies Rangan et al. (2014). To that purpose, some array antennas for the mmWave band of 5G have been proposed employing various transmission line technologies such as the traditional waveguide Kim et al. (2014), the gap waveguide Yong et al., 2020, Yong et al. 2022, Yong et al. 2023, and the substrate integrated waveguide Wu et al. (2012); Alibakhshikenari et al., 2021a, Alibakhshikenari et al., 2021b. Although these array antennas offer significantly better loss performance than conventional substrate-based array antennas for the mmWave band, they are typically bulky (due to the operating nature of the waveguide) and more expensive to manufacture. For the successful implementation and widespread deployment of the mmWave 5G band, the hardware implementation must incorporate compact, low-power, and cost-effective features.

To ensure that 5G devices can be produced on a large scale at a low cost and with a small footprint, substrate-based antennas continue to be preferred Burasa et al. (2020); Wagih et al. (2021). However, the microstrip transmission line losses must be minimised for these substrate-based antennas to operate adequately at the mmWave band. To address such requirement, one of the potential approaches is to realise the antenna on-chip Alibakhshikenari et al., 2021a, Alibakhshikenari et al., 2021b However, antennas on-chip usually suffer from high losses. To enhance the performance of the antenna on-chip, the metamaterials can be employed, but this will increase the overall fabrication complexity. Alternatively, antenna-in-package (AiP) technology, which allows active components and antennas to be combined into a single package, has led to dramatically reduced overall interconnect and transmission line losses SalarRahimi et al. (2020); Gu et al. (2019). The loss is reduced because the overall interconnect and transmission line length between the RFIC and antennas can be shortened. Various AiP designs exist in the 5G mmWave bands SalarRahimi et al. (2020); Wagih et al. (2021); Kibaroglu et al. (2018); Yin et al. (2020). However, most of these antennas only cover a portion of the vast 5G mmWave band. This may be attributed to two primary causes. First, most reported works use conventional narrowband patch antennas

SalarRahimi et al. (2020); Wagih et al. (2021); Kibaroglu et al. (2018) Although the bandwidth performance of patch antennas can be significantly enhanced by parallel-stacking two of them on two distinct substrate layers and co-optimizing the feeding network and transition design, this results in a significantly higher integration design complexity Yin et al. (2020); Kibaroglu et al. (2018). Second, the majority of analogue beamformers now available on the market cover either the N257 (26.5 – 29.5 GHz) or the N258 bands (24.25 – 27.5 GHz) Theis et al. (2021); Yin et al. (2020); Kibaroglu et al. (2018), limiting the operational frequency of the AiP. Recently, an ultra-wideband analogue beamformer with good linearity that covers the N257 and N258 bands has been proposed Alhamed et al. (2021). However, this type of beamformer is currently not widely on the market, possibly due to design complexity and cost considerations. Indeed, the current necessity of such a wideband beamformer solution remains in debate, as in most countries, either of the N257 or N258 bands, but not both, are licenced GSMA GSMA Intelligence (2021).

This work presents the wideband antenna-in-packaged (AiP) that is realised using the wideband magneto-electric dipole (MED) and integrated with two distinct commercially available analogue beamformers, one covering the N257 band and the other covering the N258 band. The MED antenna is selected in this study as the radiating element of the proposed AiP as it has been widely reported in Luk and Wong (2006); Zhai et al., 2014 as the radiating element for the design of the wideband antenna for base station application. Thus, the proposed AiP is realised using the cost-effective Panasonic Megtron-6 substrate. In this paper, the evaluation of the MED antenna's performance as an AiP will be discussed in detail. To avoid confusion in the coming discussion in this paper, the MED will be classified into four distinct categories. The design procedure of the MED AiP is summarized as follows:

- First, the conventional MED (CMED) antenna is realized. This antenna is designed and evaluated using the open boundary condition in CST Microwave Studio, making it suitable as a single-port antenna.
- Secondly, a unit cell MED (UMED) antenna is developed. Here, a single MED antenna is evaluated using the unit cell boundary condition, serving as the initial step for developing an array antenna based on the MED concept.
- Thirdly, a finite 2×2 array antenna (AMED) is designed, where the performance of the array antenna itself is considered.
- Finally, the 2×2 MED array antenna is designed with an integrated transition (IMED).

The main contributions and advantages of the proposed design approach are listed as follows:

- A 2×2 wideband active antenna-in-a-package (AiP) based on the magneto-electric dipole (MED) antenna concept has been designed, manufactured, and experimentally verified with a good agreement between measurements and simulations. The proposed solution can be used for 5G mmWave Internet of Things (IoTs) devices.
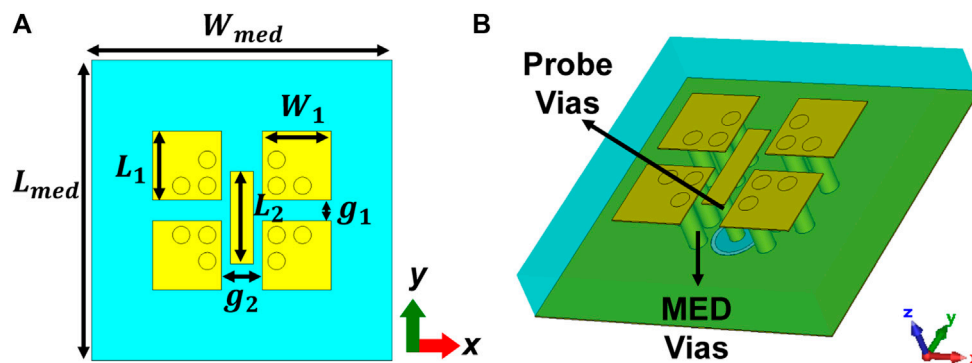
FIGURE 1
An artist of the proposed MED **(A)** Top View and **(B)** Perspective View.

- The proposed design approach has demonstrated that a single wideband radiating element can be integrated with different RFIC beamformers with limited bandwidth. This is feasible as long as the employed RFIC beamformers have the same design footprint, including the RF ports, SPI control ports, and DC power supply ports.

- The strategy for designing the transition from the beamformer to the antenna has been explained in detail, and the performance of the wideband transition has been thoroughly evaluated. This includes the choice of the transmission lines and the matching and mutual coupling considerations over the transition from the beamformer to the PCB board.

- Based on the simulation evaluation, the proposed AiP can be potentially expanded into a phased array antenna with 2D scanning performance over both E- and H-planes.

- Lastly, the proposed design approach benefits from the advantages outlined in Kibaroglu et al. (2018); Yin et al. (2020). Indeed, additional RF components, such as Wilkinson power dividers, filters, power amplifiers, etc., can be added after the common RF port of the AiP. This gives the antenna system engineer the flexibility to adapt the proposed design to the requirements of specific applications, e.g., those dictated by local authorities's requirements supporting the IoT industry.

The remainder of this article is organised as follows. In Section II, the design principle for the proposed conventional wideband magneto-electric dipole (CMED) antenna, the performance evaluation of the unit cell MED (UMED), and the 2 × 2 array antenna (AMED) are presented. Section III describes the transition design for integrating the analogue beamformer with the proposed MED array antenna (IMED). A performance comparison of the proposed AMED and IMED is also provided. Section IV presents the experimental validation of the manufactured prototype of the 2 × 2 IMED. The section also compares the proposed work and previously published antenna-in-package (AiP) designs for mmWave 5G applications, including a discussion of the advantages and disadvantages of the various approaches. In addition, recommendations for further work are provided. Section V summarises the conclusion of the presented work.

2 Design of the wideband MED array antenna

2.1 Conventional MED antenna

The design of our proposed 2 × 2 integrated array antenna for IoT applications starts with the design of a single-element passive antenna based on the conventional magneto-electric dipole (CMED) concept. The proposed CMED antenna is shown in Figure 1, where the design principle follows the approach described in Luk and Wong (2006); Li and Luk (2015). The antenna employs the Panasonic Megtron-6 substrate ($\varepsilon_r = 3.18 - 3.34$, tan $\delta = 0.004$) with a total thickness of 1.52 mm (equivalent to 0.152 λ_h, where λ_h is the wavelength at the higher operating frequency set to 30 GHz in our case). The unit cell dimension is around $W_{med} = \lambda_{cf}$, where λ_{cf} is the wavelength of the centre frequency, which is around 28 GHz. The proposed CMED antenna consists of four square patches, four sets of metalized vias, and an L-probe feeding. The four metallic square patches serve as planar electric dipoles. In addition, each set of metalized vias comprises three individual vias connected to each square patch. These, via holes and the ground plane between them, generate a vertically shorted patched antenna (also known as an equivalent magnetic dipole) that radiates through the aperture between the metallic patches. The L-shaped probe is constructed from a plated vias hole and a rectangle patch, which couple the electrical signal and excite the antenna. The main advantage of the L-probe feed is it can be easily incorporated into the antenna with thick or multi-layer substrate and can be fabricated easily. Moreover, the L-probe incorporated with the radiating MED introduces a capacitance suppressing some of the inductance introduced by the probe (metallic strip on the patch layer) thus leading to the wideband feeding performance (Mak et al., 2000). The design of the proposed CMED antenna is simulated in CST Microwave Studio with the open boundary condition. Figure 2 depicts the simulated reflection coefficient S_{11} of the proposed CMED antenna. The $S_{11} \leq -10$ dB impedance bandwidth is approximately 42.2% operating from 22 – 33.9 GHz. Furthermore, as shown in Figure 2, the CMED antenna exhibits a steady gain performance over the operating frequency, with the maximum gain G_0 ranging from 4.8 – 6.5 dBi with a variation less than 2 dBi. Figure 3 shows the simulated radiation patterns at different frequencies. The
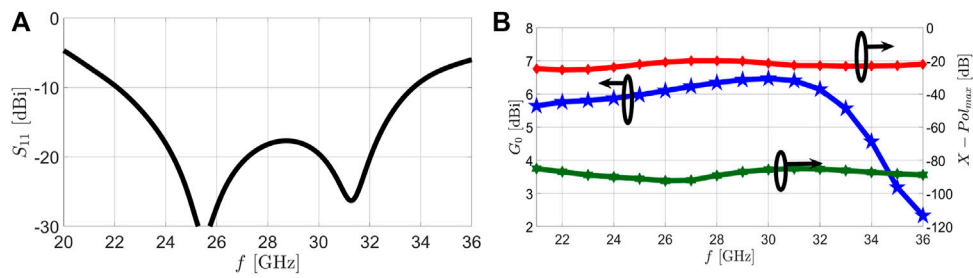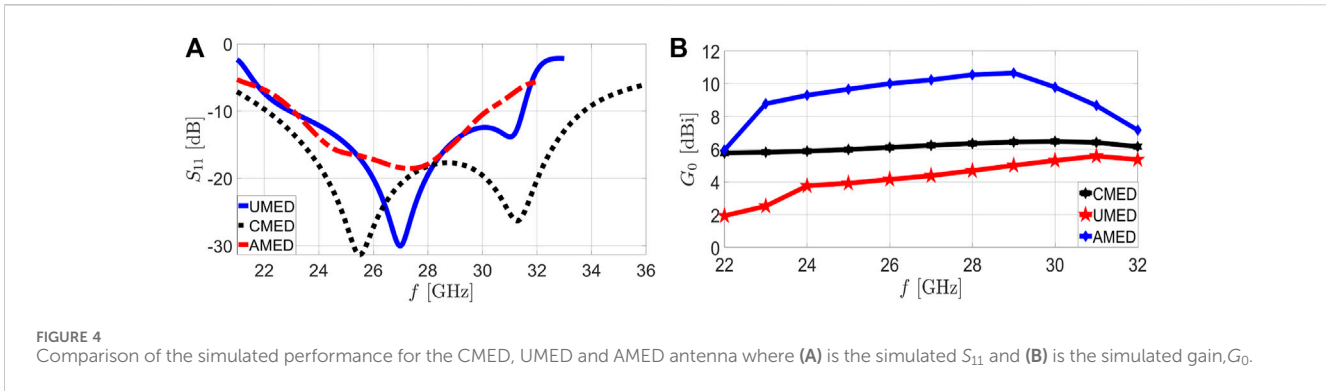
FIGURE 2
Simulated performance of the proposed CMED antenna fed by L-probe where **(A)** Simulated S_{11} and **(B)** Simulated realised gain and the maximum cross-polarisation $(X - Pol_{max})$. The red line is for the E-plane, and the green line is for the H-plane.
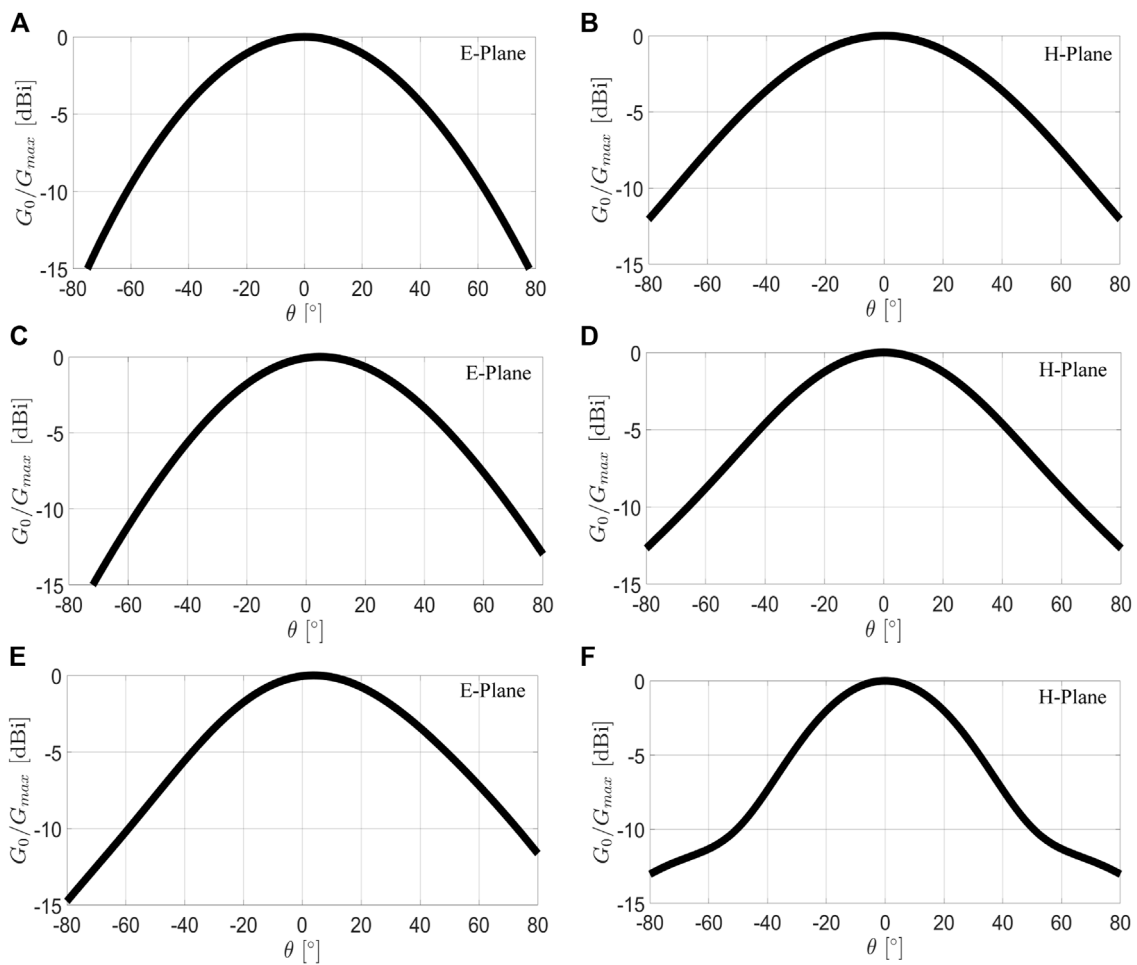
FIGURE 3
Simulated radiation pattern of the proposed CMED antenna at both E-an H-planes, where plots **(A, B)** are for 22 GHz, **(C, D)** are for 28 GHz, and **(E, F)** are for 32 GHz respectively. G_0/G_{max} is the normalized antenna gain, θ is the polar angle in degrees.

radiation patterns in the E- and H-planes are nearly identical. In addition, for both the E- and H-planes, the computed relative cross-polarisation level of the proposed CMED is below −20 dB over the bandwidth. These exceptional characteristics make it a potential candidate for developing a wideband mmWave antenna for 5G IoT applications. As stated above, array antennas are typically used when designing mmWave antennas to reduce propagation path loss. However, the proposed CMED antenna has a dimension of about λ_{cf}, which is too large for an array antenna element because of the appearance of undesirable grating lobes. Yet, it offers a solid foundation for constructing the MED array antenna element. Consequently, the following section will focus on further

FIGURE 4
Comparison of the simulated performance for the CMED, UMED and AMED antenna where **(A)** is the simulated S_{11} and **(B)** is the simulated gain, G_0.

developing the proposed CMED antenna as an element of an array antenna.
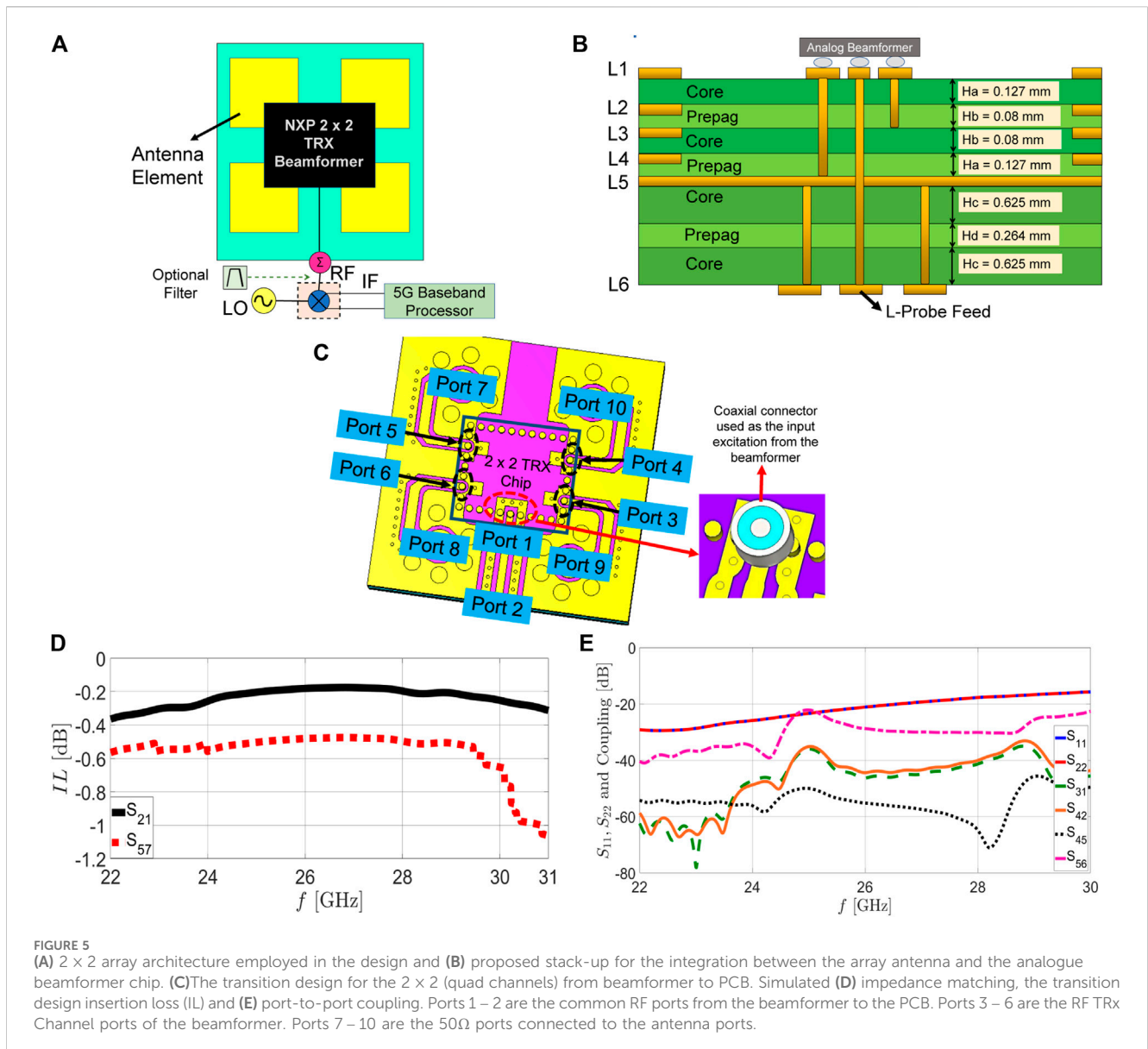
2.2 Unit cell MED and MED array antenna

The CMED design based on the design principle presented in Luk and Wong (2006); Li and Luk (2015) cannot be employed directly for array antenna design due to the large dimensions of the unit cell. The MED unit cell (UMED) dimensions need, therefore, to be adjusted to approximately $0.5\lambda_h$, where λ_h is the wavelength of the higher operating frequency. This is achieved by optimizing the UMED dimension using the unit cell boundary condition with Floquet port in the CST Microwave Studio. The ground dimension of the MED is significantly reduced in the UMED, and the distance between the dipole, g_1 and g_2 are optimized to cover as wideband as possible. Additionally, the active impedance (also known as scanning impedance when a phased array scans the beam) of the UMED antenna is evaluated using the unit cell boundary condition in the CST. The active impedance is the apparent impedance observed at the antenna element's port when operating in an array environment, and all array antenna elements are excited; Kildal (2015). This active impedance depends on the scanning angle of the phased array. This study evaluates only the broadside direction $\theta = 0°$. After the performance of the UMED has been optimized using the unit cell boundary condition, the UMED antenna is expanded into a 2×2 array (AMED, where the array impedance is evaluated using the open boundary condition). In the simulation of the active impedance of the AMED, the simultaneous excitation setting in the CST was employed to excite the 4 MED antenna elements. Figure 4A shows the comparison of the simulated S_{11} for the CMED and the impedance of UMED and AMED. Based on simulation results, the UMED has a $S_{11} \leq -10$ dB impedance bandwidth of 31.5% covering from 23.3 – 31.6 GHz, with a bandwidth reduction of approximately 15 % compared to the CMED. On the other hand, the AMED simulated based on the open boundary condition demonstrates an $S_{11,active} \leq -10$ dB bandwidth of approximately 25.2% from 23.3 – 30 GHz. As noted, the operating bandwidths of the UMED and the AMED are significantly narrower than that of the CMED antenna simulated with an open boundary condition. Several factors can explain the decrease in bandwidth. First, the unit cell size dimension of the UMED is decreased to around $0.5\lambda_h$ (to avoid the unwanted grating lobes for the array antenna). The

available space for tuning the antenna to achieve a wideband behaviour is substantially less than the CMED antenna with the element size of λ_{cf}. Moreover, in both cases, the UMED and the AMED, the mutual coupling between the neighbouring elements and the possible edge effects of the array antenna will degrade the overall bandwidth performance. Figure 4B illustrates the comparison of the simulated gain performance for the CMED, UMED, and AMED antennas. As can be seen from the simulation results, the proposed CMED demonstrates a stable gain performance of 5.6 – 6.4 dBi over the desired operating frequencies. On the other hand, the UMED shows a significant gain reduction compared to the CMED, resulting in the antenna gain varying from 3.7 – 5.6 dBi. The gain reduction of the UMED is expected because the reduction in the aperture size of the UMED will result in a drop in gain relative to the CMED. For the 2×2 AMED antenna, the gain increased to approximately 8.7 – 10.6 dBi, as expected, over the operating frequency. The proposed AMED antenna combines an analogue beamformer to produce an AiP for 5G mmWave IoT applications covering two 5G bands. To ensure the proposed AMED remained operating adequately, the transition design and the choice of the transmission lines in designing the transition from the beamformer to the AMED are critical. Its design procedures and AMED performance will be detailed in the next section.

3 2 × 2 integrated array antenna

The 2×2 active integrated array antenna, whose architecture is shown in Figure 5A, is realised by integrating the proposed AMED with two distinct analogue beamformer chips, i.e., the *MMW9002KC* and the *MMW9004KC* chips. Integrating the array antenna with the analogue beamformer consists of three main steps: (i) design of the RF operation part, (ii) design of the circuit for serial peripheral interface (SPI) control of the analogue beamformer, and (iii) design of the circuit for the analogue beamformer's DC power supply. Each of these parts is designed separately in different substrate layers. In our proposed stack-up shown in Figure 5B, L1 and L2 are used for the RF layer, L3 is used for SPI control, L4 is used for the DC power supply, and L5 and L6 comprise the antenna layer. It is worthwhile noting that, in considering the fabrication, the antenna layer (L5-L6) consists of two core layers and one prepreg layer to improve the overall substrate stack-up symmetry from L1 to L6 layers and avoid undesirable substrate bending. Further, the

FIGURE 5
(A) 2 × 2 array architecture employed in the design and (B) proposed stack-up for the integration between the array antenna and the analogue beamformer chip. (C)The transition design for the 2 × 2 (quad channels) from beamformer to PCB. Simulated (D) impedance matching, the transition design insertion loss (IL) and (E) port-to-port coupling. Ports 1 − 2 are the common RF ports from the beamformer to the PCB. Ports 3 − 6 are the RF TRx Channel ports of the beamformer. Ports 7 − 10 are the 50Ω ports connected to the antenna ports.

discussion is focused only on the RF transition part. The SPI control and DC power supply circuit can be designed using the recommendations in the analogue beamformer data sheet (not publicly available, but can be requested from NXP).
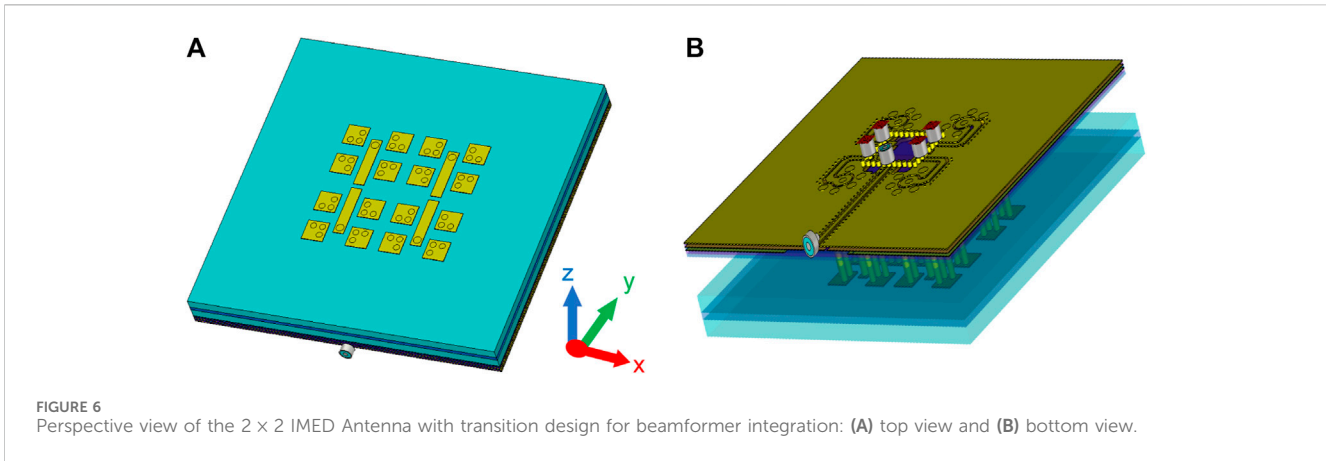
3.1 2 × 2 TRX beamformer chip

As stated above, our challenge is to combine two different beamformers with the proposed MED to form the integrated array antenna. The two analogue beamformers cover a part of the 5G FR2 mmWave band with high linearity performance. The *MMW9004KC* operating from $24.25 − 27.5$ GHz and the *MMW9002KC* working from $26.5 − 29.5$ GHz, respectively. Thanks to the unique packaging technology employed, each beamformer has the same chip dimensions and unique RF input/output ports, as well as the ports for SPI and DC power supply, making integration with the wideband array antenna with two

different chips possible. Moreover, both beamformers comprise five RF input/output ports, which include $2 × 2$ (quad) transmit/receive (TRx) channels and one for the power combiner/divider coming from four channels. Furthermore, all five RF ports are terminated with a 50Ω, which eases the antenna integration and transition design. The SPI controls the beamformer's gain, phase, and bias current settings.

3.2 Transition design

In the design of the transition from the analogue beamformer to the AMED antenna, two crucial aspects must be taken into account: (i) a good impedance matching over the intended operating frequency for the transition network between the beamformer and the AMED antenna and (ii) a low mutual coupling between the input/output RF ports of the beamformer at the PCB. Unlike the conventional MED AiP presented in Kuo et al. (2022), which

FIGURE 6
Perspective view of the 2 × 2 IMED Antenna with transition design for beamformer integration: **(A)** top view and **(B)** bottom view.

focused only on antenna design, the matching design focuses on the conventional antenna matching technique, where the antenna feeding can be joint tuning with the antenna to obtain the required matching performance and terminated with RF connector. However, this flexibility is absent in an AiP with an active beamformer integrated because the transition design should consider the active beamformer's packaging. Thus, this section outlines the procedures for designing the transition layer from the beamformer to the antenna. As explained in the previous section, the analogue beamformer only promises good linearity over the frequency band from 24.25 – 29.5 GHz. Thus, in our design process, we will focus on optimising the performance over this range, although the proposed MED antenna could operate at a wider bandwidth. The transition design for the 2 × 2 (quad channels) from beamformer to PCB is shown in Figure 5C. The transition from the analogue beamformer's common RF port (Port 1 in Figure 5C) to the PCB is designed and evaluated. As illustrated in Figure 5C, the coplanar waveguide (CPW) transmission line with ground-signal-ground (GSG) characteristics is utilized. The open boundary condition in the CST is employed in the design of the transition from the beamformer chip to the PCB. Moreover, 36 metallic vias were modelled to represent the input/output of the RFIC beamformer and excited using a coaxial port that covers the GSG of the RF input port. All the coaxial port covers the GSG RF input port are modelled as 50Ω. To obtain a wideband transition with a good matching level, the CPW transition lines width and the vias connecting the transition layer to the antenna layer as illustrated in Figure 5C are tuned and optimized. As can be seen from Figure 5, the coplanar waveguide transmission lines from the output of the beamformer to the vias connecting to the L-probe antenna feeding are being tapered to ensure wideband transition performance. As can be seen from Figures 5D,E, the simulation shows that a good impedance matching from the common port to the PCB is achieved with the S_{11} and S_{22} below −15 dB throughout the operating bandwidth. On the other hand, the simulated insertion loss (IL) for the transition design was $S_{21} \geq −0.4$ dB for the RF common port over the desired operating frequency. Moreover, the simulated IL for the transition from the RFIC beamformer to the antenna was $S_{57} \geq −0.6$ dB. Since the transition design from the beamformer RF port to the antenna port is identical to the other elements, their IL is identical. In addition, the port-to-port coupling is evaluated. As can be seen, the S_{56} has the worst coupling, as the energy from two

RF ports on the beamformer into the PCB is coupled to each other. The simulated mutual coupling among other ports remains better than 40 dB over the operating bandwidth, which is sufficiently low. The transition layer and the MED antennas are then combined to form the antenna-in-package (AiP) as illustrated in Figure 6.

3.3 Performance evaluation of the integrated MED

After completing the transition design, it is essential to evaluate the performance of the proposed IMED, including the additional RF transition layer and the additional substrate layers for digital and DC power circuits, which are integrated into a single package. Figure 6 illustrates the proposed 2 × 2 IMED antenna with the integrated transition. The open boundary condition in the CST Microwave Studio is used to evaluate the active impedance and radiation pattern of the proposed IMED antenna. Figure 7A compares the simulated S_{11} of the proposed AMED and IMED. As observed, the proposed AMED and IMED have been adequately impedance-matched. Nonetheless, it is essential to note that, with the transition design incorporated, the IMED array slightly improves the matching performance. This improvement can be explained by tuning enhancement and optimization flexibility in the RF transition layer. Indeed, in the case of AMED, only the L-probe feeding (rectangular patch and metalized vias dimensions) can be adjusted for optimisation. On the other hand, when the transition layer is integrated into the IMED, additional CPW transmission lines can be employed to optimise the antenna matching performance jointly. In addition, Figure 8 illustrates the comparison of the simulated radiation patterns for the proposed AMED and IMED array antennas in the E- and H-planes, respectively, at different frequencies. As can be seen, the simulated radiation patterns are identical for both antennas. This suggests that the transition design is performed adequately to provide a good transition matching between the RFIC beamformer and the antenna elements. Thus, it has no substantial influence on the performance of the MED antenna. This observation is also reflected in the simulated gain performance as illustrated in Figure 7B. The simulated gain performance of the AMED and IMED antennas are nearly identical. A slight variation of approximately 0.3 − 0.5 dB results
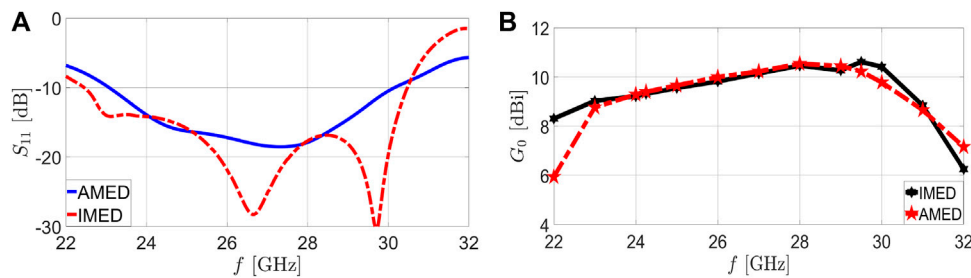
FIGURE 7
Comparison of the simulated performance of the proposed 2 × 2 MED Array with and without the transition design with **(A)** the simulated S_{11} and **(B)** the simulated gain, G_0. The IMED indicates the MED with transition design for integration with the analogue beamformer, and AMED is the array of the MED only.

from the additional dielectric losses of the IMED and/or the difference in the impedance-matching performance of IMED and AMED.

4 Results and discussion

To validate the proposed solution, two identical IMED antennas were manufactured utilising the standard multilayer PCB fabrication technology. Figure 9 shows one of the fabricated IMED prototypes. It is worthwhile to note that the prototypes for the N257 and N258 bands are identical, except for the integrated analogue beamformers. Although not depicted in Figure 9, it is important to note that an additional DC power supply unit and control board are required to provide the supply and to control the amplitude and phase of the beamformer, respectively.

Our prototypes demonstrate the proposed 2 × 2 array layout, which is unconventional (with the two bottom elements mirroring relative to the E-plane (yoz−plane)) but symmetrical. This is done to customise the array design for easier RFIC integration, resulting in a 180° phase difference between the top and bottom elements. By altering the operational phase of the beamformer, this 180° phase mismatch may be adjusted thanks to the phase-shifting capability of the RFIC.

4.1 Radiation pattern and EIRP measurements

The fabricated IMED prototype is characterised in the far-field using a vector network analyzer and a standard horn antenna using the anechoic chamber in Gapwaves AB, Sweden. It is worthwhile to mention that even though all considerations for reducing systematic errors were addressed during the measurement campaign, a discrepancy of ± 0.5 dB was anticipated for the measurement results. This discrepancy is primarily attributable to the limitations of our measurement setup, including angular misalignment between the antennas, extra disturbances from the measurement equipment, and temperature drift of the RFICs. The normalised radiation patterns for both fabricated IMED antennas were measured in a fixed configuration, allowing for a fair comparison of

measurements. Figure 10 compares the measured and simulated radiation patterns at various frequencies for the proposed IMED integrated with the *MMW 9004 KC* analogue beamformer. On the other hand, the comparison of the measured and simulated radiation patterns at different frequencies for the fabricated IMED with *MMW 9002 KC* is shown in Figure 11. As can be seen, for both fabricated prototypes, the measured radiation patterns are identical to the simulations. Nevertheless, the additional ripples observed in the measured radiation pattern are mainly due to the limitations of our measurement setup, which is not completely shielded.

Figures 12A,B depict the measured effective isotropic radiated power (EIRP) of manufactured IMED with the two different integrated analogue beamformers. The IMED with *MMW 9004 KC* achieved the 1 dB compression point ($P1dB$) and the saturation at 35.3 dBm and 37.5 dBm (P_{sat}), respectively, at $f_c 26$ GHz. On the other hand, corresponding results for the IMED with *MMW 9002 KC* are 35.1 dBm for the $P1dB$ while P_{sat} is attained at $f_c = 28$ GHz. The agreements between measured EIRP are in good agreement with the theoretical design values for both IMEDs integrated with *MMW 9004 KC* and *MMW 9002 KC*. The theoretical values were estimated based on the following equations

$$EIRP_{P1dB} \approx P1dB_{BFIC} + G_{subarray} + 20\log_{10}(N), \quad (1)$$

where $EIRP_{P1dB}$ is the EIRP of the IMED array antenna at $P1dB$, the $P1dB_{BFIC}$ is the beamformer IC (BFIC) output power at $P1dB$, $G_{subarray}$ is the gain of the subarray antenna including the feed, ohmic and mismatch losses, and N is the number of the antenna elements. For the IMED integrated with *MMW 9004 KC*, the $EIRP_{P1dB} = 36.2$ dBm at $f_c = 26$ GHz was obtained with $P1dB_{BFIC} = 20$ dBm, $G_{subarray} = 4.2$ dB, and $N = 4$. For the IMED with the *MMW 9002 KC*, the $EIRP_{P1dB} = 35.7$ dBm was computed at $f_c = 28$ GHz with $P1dB_{BFIC} = 19$ dBm, $G_{subarray} = 4.7$ dB, and $N = 4$, and are computed using Equation 1. While the measured results are comparable to the theoretical values, the minor differences could result from higher losses due to the IMED array antenna manufacturing imperfections. Figures 12C,D illustrate the measured EIRP at $P1dB$, and the saturation level of the two fabricated IMED at different frequency points. For IMED with *MMW 9004 KC*, the measured EIRP at $P1dB$ is equal to 34.8,
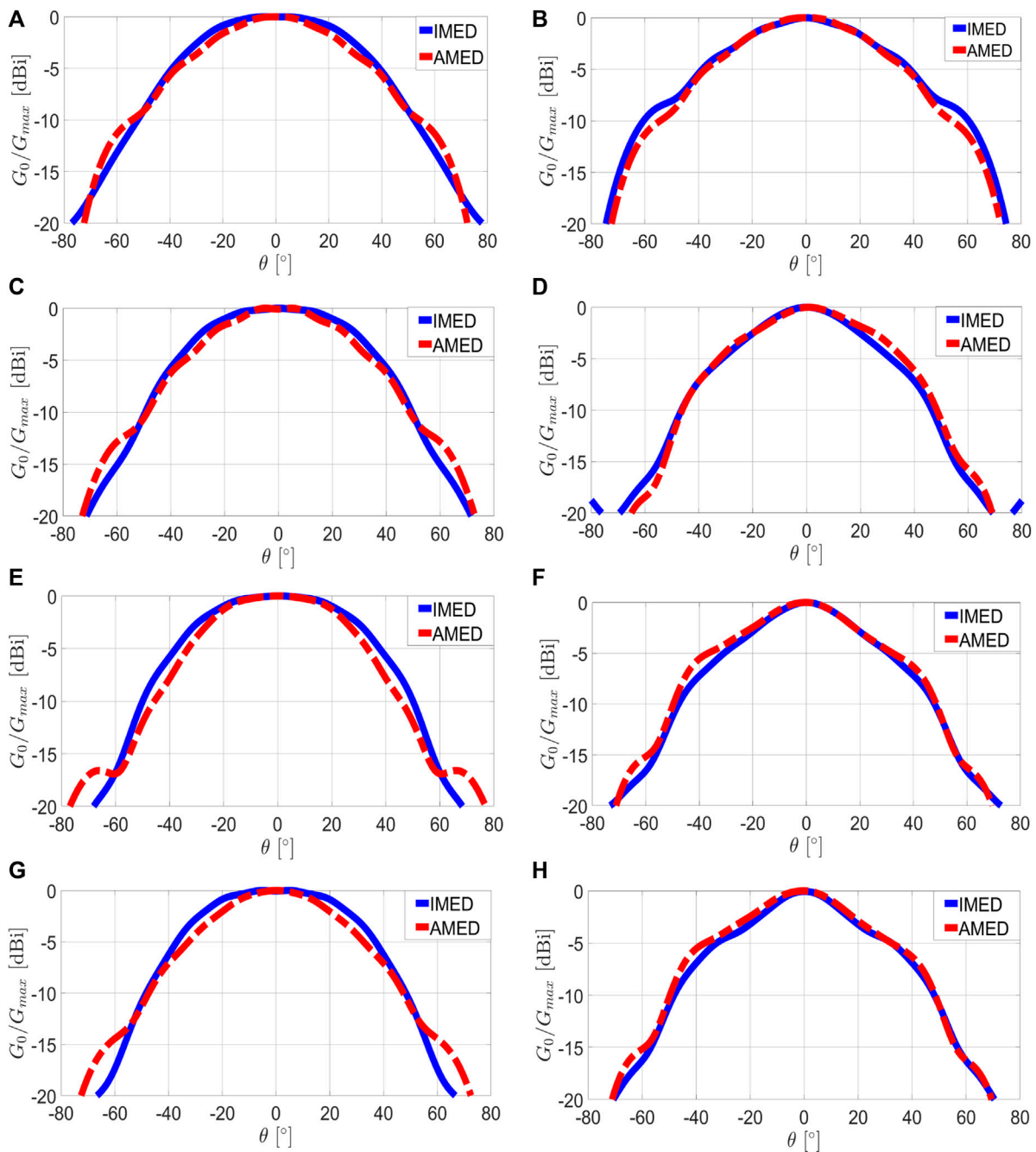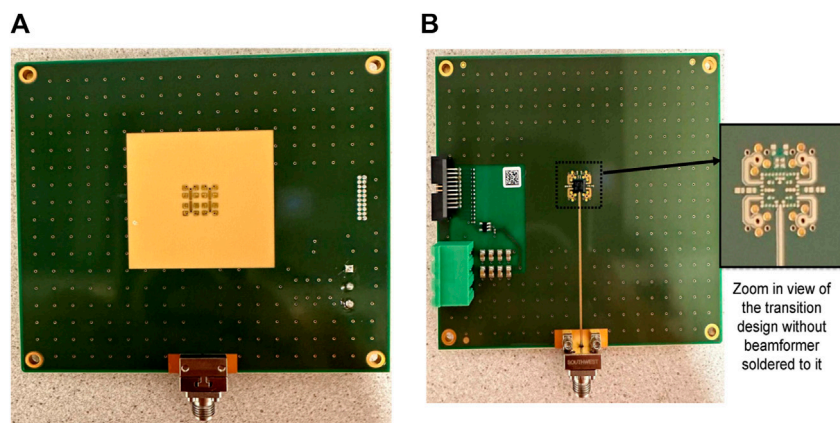
FIGURE 8
Comparison of the simulated radiation pattern of the AMED and IMED. Results are depicted at different frequencies: 24.25 GHz at the E-plane in **(A)** and the H-plane in **(B)**, 26 GHz at the E-plane in **(C)** and the H-plane in **(D)**, 28 GHz at the E-plane in **(E)** and the H-plane in **(F)**, and 29.5 GHz at the E-plane in **(G)** and the H-plane in **(H)**.

35.4 and 36.1 dBm at 24.25, 25 and 27.5 GHz, respectively. The maximum EIRP at these frequencies are 36.9, 37.4, and 37.7 dBm, respectively. On the other hand, the IMED with *MMW 9002 KC* achieved the EIRP at $P1dB$ of 34.7 dBm, 34.9 dBm and 35.5 dBm at 26.5, 27 and 29.5 GHz. The maximum EIRP at these frequencies equals 37.4 dBm, 37.7dBm, and 37.9dBm, respectively. Moreover, the measured relative cross-polarization level of both manufactured IMEDs is always lower than −20 dB, as illustrated in Figures 12C,D.

4.2 Evaluation of the scanning capability of the proposed IMED as the phased array antenna

Theoretically, suppose the suggested UMED antenna is appropriately designed (with unit cell dimensions around $\leq 0.5\lambda_h$). In that case, it might be extended to a larger array antenna with beam scanning capability. As demonstrated in

FIGURE 9
Perspective view of the fabricated 2 × 2 IMED: **(A)** top view and **(B)** bottom view. The black dotted lines is the beamformer chips (either *MMW 9002 KC* or *MMW 9004 KC*).
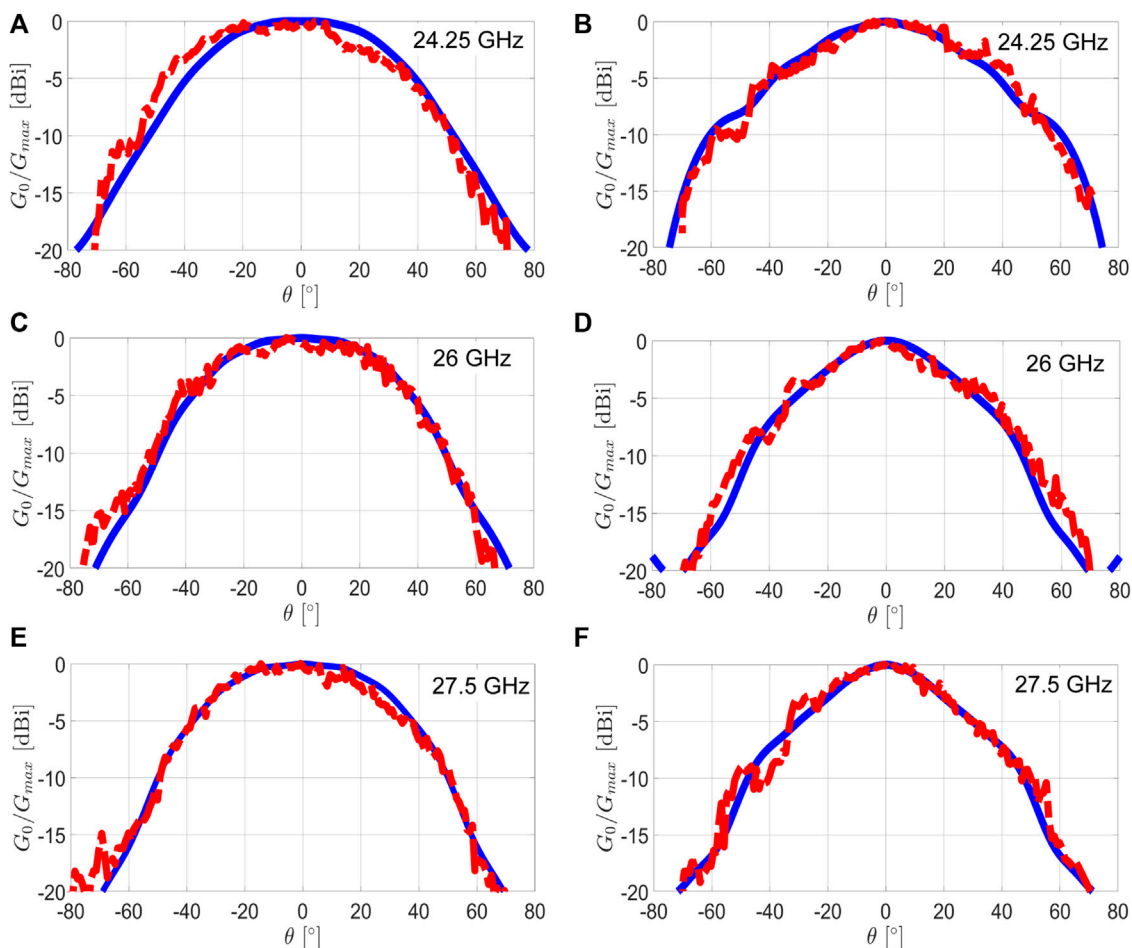
FIGURE 10
Comparison of the simulated and measured radiation patterns of the AMED and IMED. Results are depicted at different frequencies: 24.25 GHz at the E-plane in **(A)** and the H-plane in **(B)**, 26 GHz at the E-plane in **(C)** and the H-plane in **(D)**, and 27.5 GHz at the E-plane in **(E)** and the H-plane in **(F)**.
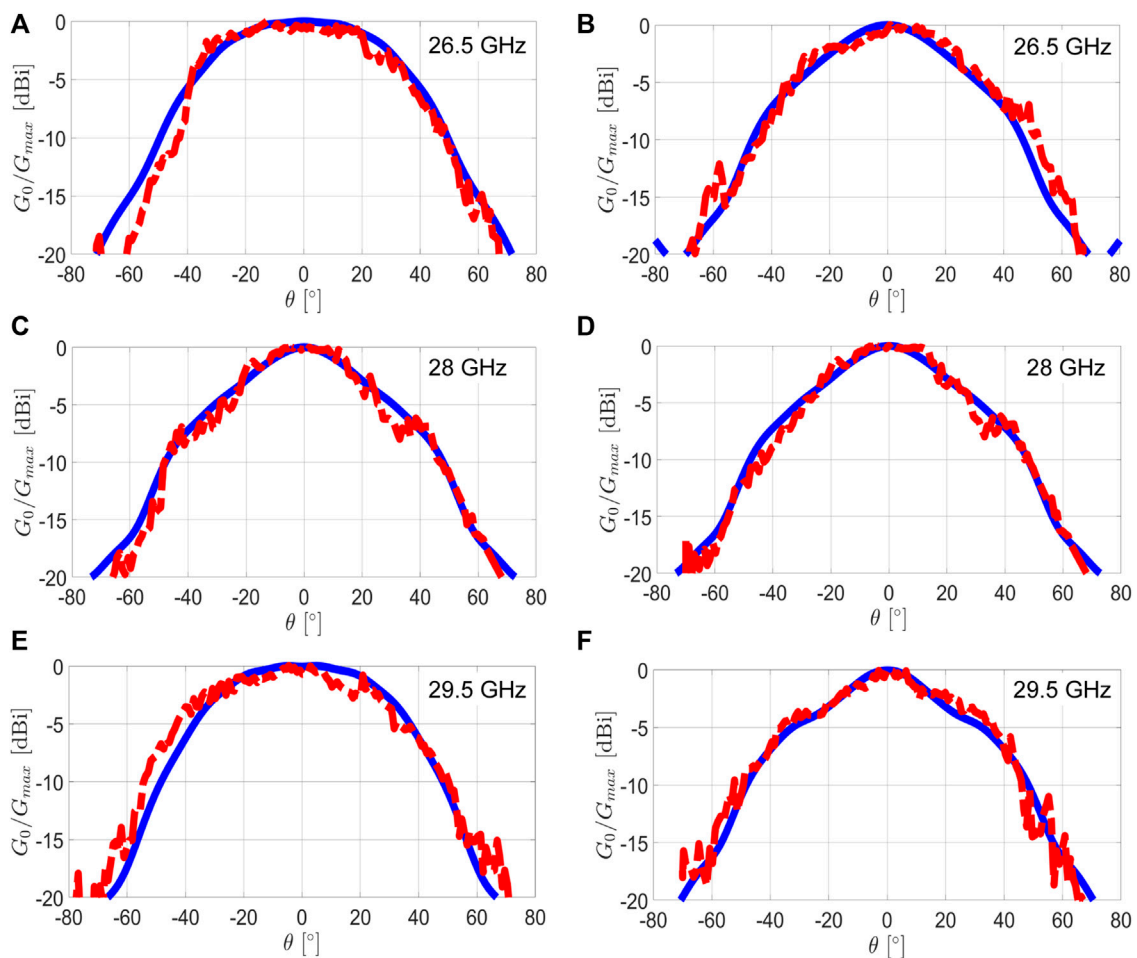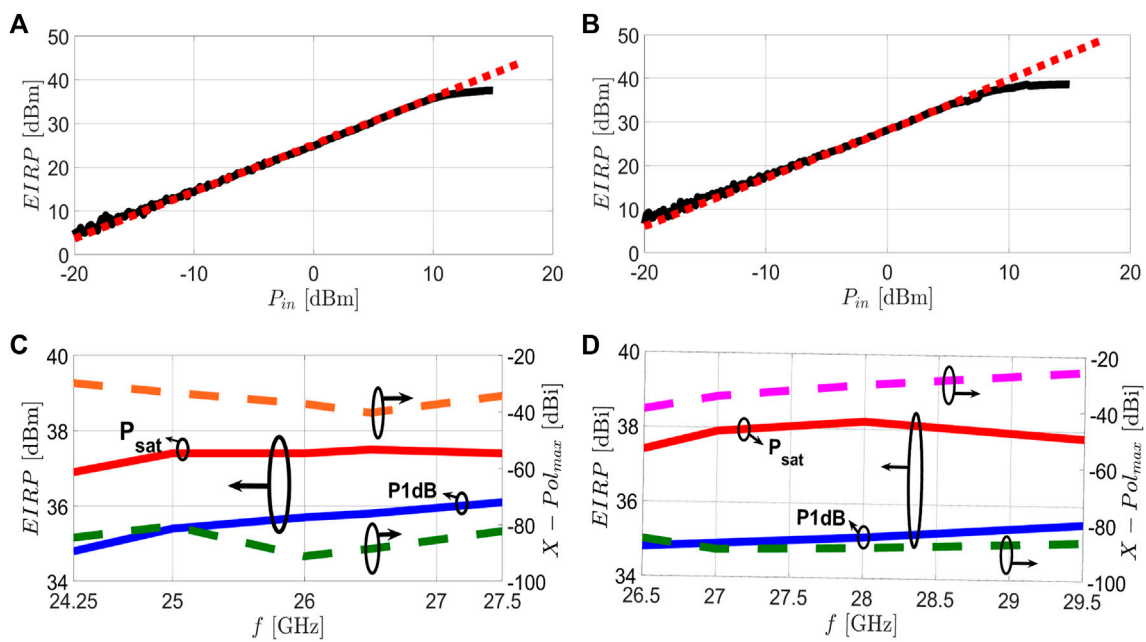
FIGURE 11
Comparison of the simulated and measured radiation patterns of the AMED and IMED. Results are depicted at different frequencies: 26.5 GHz at the E-plane in **(A)** and the H-plane in **(B)**, 28 GHz at the E-plane in **(C)** and the H-plane in **(D)**, and 29.5 GHz at the E-plane in **(E)** and the H-plane in **(F)**.

Kibaroglu et al. (2018), the key advantage of the architecture presented in Figure 5 allowed the extension to a larger array antenna to be accomplished easily by arraying the designed IMED in the design with an additional Wilkinson power divider connecting between one to another beamformer used to control the amplitude and phase input to the antenna Kibaroglu et al. (2018). Thus, its scanning capability must be evaluated to ensure that our developed MED can be extended as a phased array antenna with beam scanning capability. First, the unit cell boundary condition in the CST Microwave studio is employed to evaluate the scanned image (sometimes also known as active image) of the proposed UMED. The computed scanning impedances for both E- and H-planes scanning of the proposed UMED antenna are depicted in Figure 13. The proposed MED phased array antenna is intended to operate from 24 − 30 GHz with acceptable degradation of the scanning impedance from −10 dB to −7 dB, which is equivalent to an additional 0.5 dB gain drop due to the mismatching caused by beam scanning Hansen (2009). For instance, with a scanned impedance of −10 dB, the power loss due to the mismatch is approximately 0.5 dB and is increased to 1 dB when the scanned impedance has deteriorated to −7 dB. The power loss due to the beam

scanning mismatching can be computed using mismatch loss, $L_{mismatch} = 1 − |\Gamma|^2$, where Γ is the reflection coefficient Pozar (2011). considering the operating frequency of 24 − 30 GHz, in the E-plane scanning, the proposed UMED can only scan up to 50° at $S_{11,scanned} \leq − 7$ dB. On the other hand, in the H-plane scanning, the proposed UMED could only support the scanning up to 40°. This observed mismatching in the $S_{11,scanned}$ is mainly due to the variation of the mutual coupling of the phased array when the beam is scanned away from the broadside Hansen (2009). Moreover, this mismatching might be due to the propagation of the unwanted surface waves within the dielectric substrate Hansen (2009).

As well known, the performance of the centre elements can be approximated reasonably well by an infinite array model. However, in realistic array antennas with a finite number of antenna elements, the edge element patterns, and scanned reflection coefficients, $S_{11,scanned}$ will suffer from inaccuracies due to the asymmetric environment. Therefore, to further investigate the beam scanning performance of the proposed MED phased array antenna, an 8×8 finite array antenna is simulated in CST Microwave Studio with an open boundary condition. Since the proposed MED antenna was evaluated using the unit cell boundary condition in the previous

FIGURE 12
The measured EIRP at the broadside direction ($\theta = 0°$) of the 2 × 2 IMED with **(A)** *MMW 9004 KC* measured at 26 GHz and **(B)** *MMW 9002 KC* measured at 28 GHz. Also shown are the EIRP and relative cross-polarization level ($X - Pol$) in the broadside direction ($\theta = 0°$) of the 2 × 2 IMED with **(C)** *MMW 9004 KC* and **(D)** *MMW 9002 KC* measured at different frequencies.
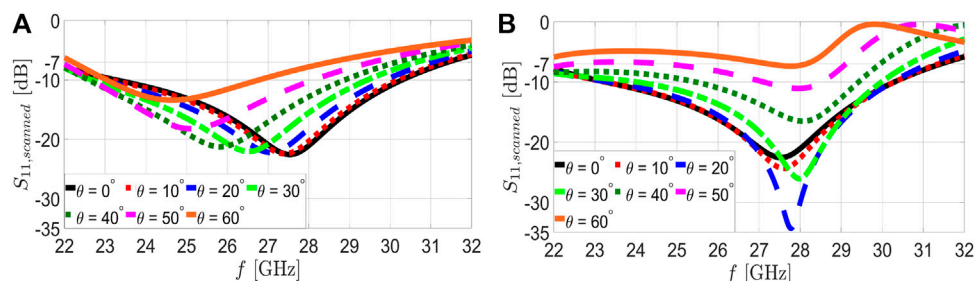
FIGURE 13
Computed scanning impedance $S_{11,scanned}$ of the proposed unit cell MED antenna fed by L-probe as a function of the frequency for different scanning angles θ with **(A)** for E-plane scanning and **(B)** for H-plane scanning.

investigation, for finite array antenna, to minimise the undesirable edge effects, an additional row/column of dummy elements is added to each side of the 8 × 8 array layout.
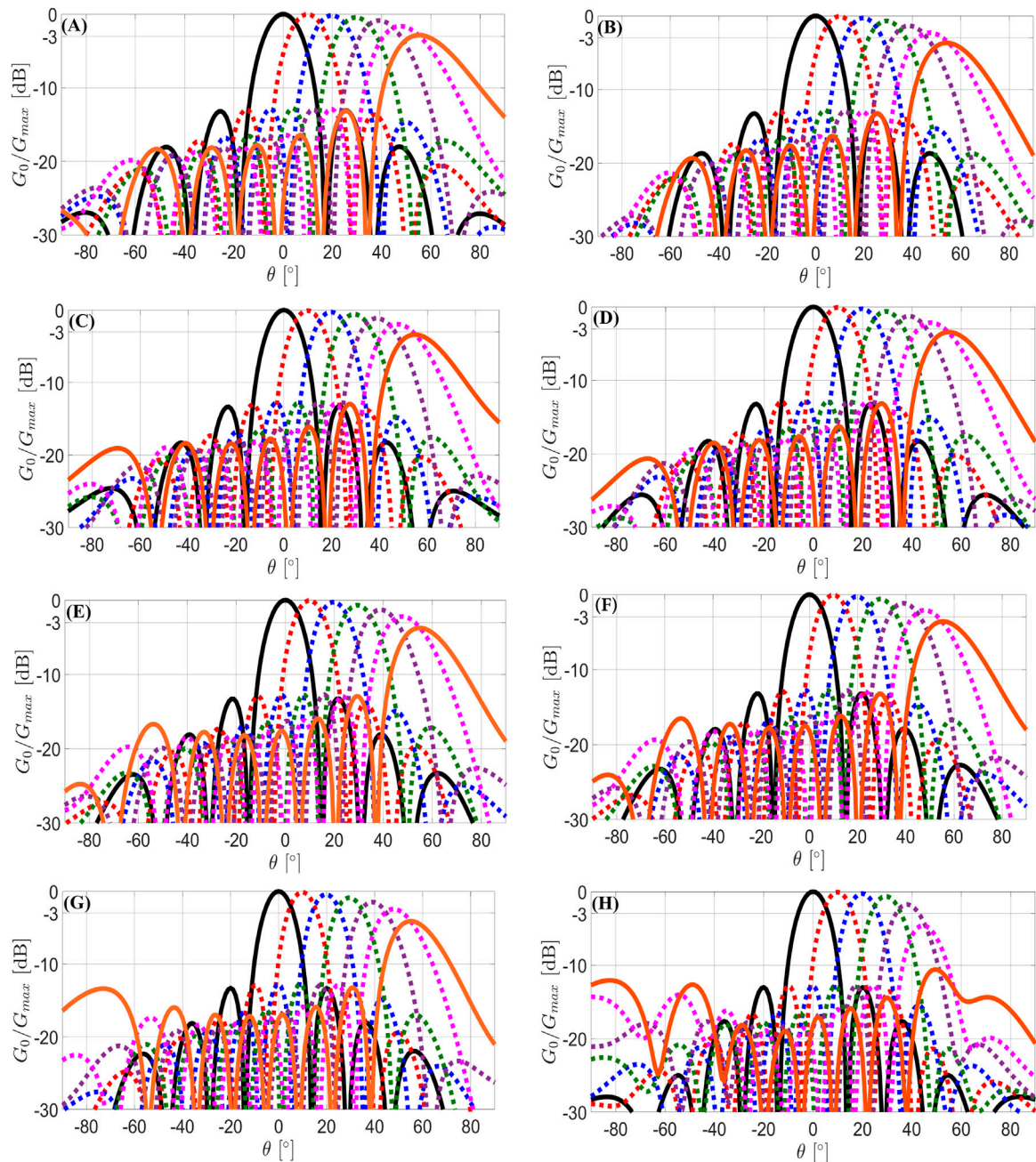
Figure 14 show the computed radiation pattern of the proposed 8 × 8 MED phased array antennas at 24 GHz (lower end of the targeted operating frequency), 26 GHz, 28 GHz and 29.5 GHz (higher end of the targeted operating frequency). Results are provided for scanning in the E- and the H-planes. Several relevant observations can be drawn from the computed radiation patterns. First, considering a 3 dB loss in gain when the radiation beam is scanned away from the broadside direction, the considered MED phased array exhibits better scanning performance at the E-plane than at the H-plane. It is worthwhile noting that this effect is more significant at the 29.5 GHz than at 24 GHz. This is explained by the fact that

the wavelength at 29.5 GHz is closer to the maximum allowed inter-element distance, avoiding the appearance of grating lobes given by

$$W_{\text{MED}} \leq \frac{\lambda_{\text{h}}}{1 + \sin \theta_{\text{scanning}}}, \quad (2)$$

where the λ_{h} is the wavelength of the highest operating frequency of interest, i.e., $f_{\text{h}} \approx 30$ GHz for the targeted design, and θ_{scanning} is the scanning angle. This results in a more significant mismatching of the phased array antenna impedance. This finding is consistent with the conclusion based on the computed scanning impedance of the MED unit cell phased array shown in Figure 13. Indeed, a better scanning impedance matching is achieved for the E-plane scanning (up to ± 50°) as compared to the H-plane scanning (up to ± 40°) of the proposed MED phased array antenna.

FIGURE 14
Computed normalised radiation pattern of the proposed IMED with 8 × 8 array configuration. Results are depicted at different frequencies: 24.25 GHz at the E-plane in (A) and the H-plane in (B), 26 GHz at the E-plane in (C) and the H-plane in (D), 28 GHz at the E-plane in (E) and the H-plane in (F), and 29.5 GHz at the E-plane in (G) and the H-plane in (H).

Another key parameter of the radiation performance of the phased array antenna is the side lobe levels (SLLs). It is worth noting that, in the broadside direction, the SLLs of the proposed MED array antenna are as low as −13 dB for both E- and H-planes. Nevertheless, an intriguing observation can be made when the beam is scanned away from the broadside. At the low-end frequency (24 GHz), the SLLs of the proposed MED phased array are approximately −11.3 dB and −11.6 dB for E- and H-planes, respectively. However, at higher operating frequencies (29.5 GHz), the SLLs are worse than at lower-end

frequencies, with SLLs approximately −10.6 dB and −11.1 dB for both E- and H-plane scanning, respectively.

4.3 Discussion

Table 1 compares the proposed IMED and the currently published AiP or integrated antenna operating at mmWave bands. Our proposed method demonstrates the feasibility of realizing a low-cost AiP with two distinct active beamformers

TABLE 1 Performance comparison of existing AiP for mmWave applications. f is the operating frequency, and EIRP is the effective isotropic radiated power. [Ref.1] is SalarRahimi et al. (2020), [Ref.2] is Kibaroglu et al. (2018), [Ref.3] is Hwang et al. (2019), [Ref.4] is Gu et al. (2021), [Ref.5] is Kuo et al. (2022), [Ref.] is Jang et al. (2023), and [Ref.7] is Chou et al. (2021), respectively.

Ref.	This work	[Ref.1]	[Ref.2]	[Ref.3]	[Ref.4]	[Ref.5]	[Ref.6]	[Ref.7]
f [GHz]	24.25– 29.5	25.8– 29.8	28.5– 30.5	26.3– 29.75	24.25– 29.5	135.4– 158.8	56.4– 69.5	26.5– 29.5
Antenna Choice	MED	Patch	Patch	Quasi Yagi	MED	MED	E- Patch	Dipole
Unit Cell Dimension [λ_0^2]	0.51 × 0.51	0.5 × 0.5	0.5 × 0.5	0.5 × 0.25	0.51 × 0.51	1 × 1	0.48 × 0.48	2.24 × 0.35
Polarisation	Single	Single	Single	Single	Dual	Single	Single	Dual
IBW%	19.5	14.4	6.8	12.3	19.5	15.9	20.8	6.1 − 21.4
Array Size	2 × 2	2 × 2	2 × 2	1 × 4	2 × 2	4 × 2	2 × 2	1 × 4
G_0 [dBi]	≥ 8.5	≥ 5.5	N/A	≥ 8.9	≥ 5	≤ 14.1	≤ 12	≤ 9.2
EIRP @ P_{P1dB} [dBm]	35.3 (at 26 GHz) 35.1 (at 28 GHz)	N/A	24.5	N/A	N/A	N/A	N/A	N/A
No.of Substrate Layers	6	4	4	10	13	3	10	18
Substrate Material	Megtron −6	RO 4003C	RO 4350B	IS 300MD	Organic Built-up	BT-based organic	GFPL- 970LF	LTCC
Design Complexity	Low	Low	Medium	Low	High	High	Low	Medium

incorporated that operate at different frequencies utilizing a single wideband MED antenna with the same transition design included. Moreover, this can be realized using the cost-effective dielectric substrates commonly employed in the industry while providing adequate radiating performance. Compared to the AiP published in Table 1, all these proposed AiP solutions share one common feature: all are realized based on multilayer stack-up substrates. The table shows that the PCB stack-up complexity is closely related to the polarization (single or dual) the AiP supports. In general, the dual-polarization AiP requires more substrate layers as the antenna feeding design is much more complex compared to a single-polarized antenna.

Furthermore, to achieve AiP with wideband performance, the patch antenna SalarRahimi et al. (2020); Kibaroglu et al. (2018); Jang et al. (2023), dipole antenna Hwang et al. (2019); Chou et al. (2021), and MED antenna Gu et al. (2021); Kuo et al. (2022) are widely used as radiating elements. Patch antennas are among the most popular radiating elements because they offer a straightforward and inexpensive design. Despite this, patch antennas SalarRahimi et al. (2020); Kibaroglu et al. (2018); Jang et al. (2023) typically support a somewhat limited bandwidth. Additional cutting is necessary to improve these patch antennas' bandwidth and matching performance. For example, in SalarRahimi et al. (2020), a circular slot is cut

across the rectangular patch to improve bandwidth performance, while in Jang et al. (2023), the rectangular patch is modified to an E-shaped patch. The end-fire dipole antenna Hwang et al. (2019); Chou et al. (2021) is another common radiating element used in developing AiP for the same reason as patch antennas. In developing the AiP, the dipole antenna demonstrates a good bandwidth and radiation performance. However, due to the non-planar characteristics, it can only be used to create a linear array AiP. In addition, AiP based on end-fire dipole antennas typically requires more substrate layers, resulting in a significantly more complex fabrication process and higher production costs. Due to its promising bandwidth and radiation performance, a growing interest in using the magneto-electric dipole (MED) Gu et al. (2021); Kuo et al. (2022) antenna has been growing in developing the AiP. As shown in Table 1, MED antennas often offer a substantially wider bandwidth performance while featuring a slightly larger number of substrate layers than microstrip patch antennas. Similar features are observed in our suggested MED design, which supports an impedance bandwidth up to 19.5% with 6 layers of the dielectric substrates. However, compared to Gu et al. (2021), our proposed MED has higher gain performance with the same unit cell dimension. Moreover, compared to the AiP proposed in Kuo et al. (2022), our proposed MED solution

can be realized using the conventional dielectric substrate commonly employed in the industry.

As mentioned above, the introduction of AiP aims to reduce transmission line loss between the antenna and the RFIC. Nevertheless, it is worth noting that most of the works presented in Table 1 have not considered the impact of the integration with the RFIC. Most of the earlier development of the AiP was targeted toward optimizing the improved radiating performance and manufacturability of the proposed AiP. However, when RFIC integration is considered, the design and fabrication process will have to consider additional aspects of the microwave circuit performance, limiting the design flexibility of the AiP and affecting its overall performance. For instance, without the integration of the RFIC beamformer, the AiP is designed following the conventional antenna design approach using the microstrip line and terminated the antenna port using the RF connector Hwang et al. (2019); Kuo et al. (2022). Nevertheless, the design flexibility is later limited to only the CPW transmission line when the RFIC is integrated. Moreover, the performance of the AiP will also be limited by the performance of the RFIC, which is usually not considered in these AiP designs. Among the earliest works that considered the integration of the RFIC and the antenna performance is the work reported in Kibaroglu et al. (2018). However, due to the limited bandwidth use of the patch antenna and RFIC, the suggested AiP can only deliver an operating bandwidth of 2 GHz, with an EIRP at P1dB of 24.5 dBm. In the subsequent work presented in SalarRahimi et al. (2020), RFIC integration was also considered. However, the focus of the work was on the characterization of the passive antenna after the additional RF network for the transition of the RFIC to the antenna has been added to the antenna package. Hence, the performance of the AiP, including the EIRP performance, was not reported when the RFIC was turned on. Similar to the work provided in Jang et al. (2023), the RFIC is integrated into the design process, and the scanning capabilities of the proposed solution are evaluated. However, the manufactured antenna was only passively measured, and no EIRP performance was reported.

To the authors' best knowledge, no AiP based on MED has been proposed and investigated to integrate with two distinct active beamformers. Therefore, in our presented study, we have investigated the performance of the AiP when the RFIC is integrated with the proposed MED array antenna. The CST simulation evaluated the passive AiP performance, including gain and impedance matching. The manufactured IMED antenna is characterized by the operation of the RFIC and the measurement of EIRP performance. Notably, this study did not give several essential characteristics of the AiP, such as the power consumption of the AiP at different input powers and the power consumption at Tx and Rx modes, since they are intimately related to the operation of the RFIC. However, as the development of the RFIC is not part of the contribution of the presented study and the power consumption at various scenarios of the RFIC is accessible in the NXP data sheet (can be obtained by request to NXP), it is not reported in our paper.

5 Conclusion

This paper presents an antenna-in-package (AiP) design for mmWave 5G applications based on the 2×2 wideband magneto-electric dipole (MED) antenna concept. The proposed solution is a potential candidate for the Internet of Things (IoTs) applications operating at the mmWave 5G. The proposed MED antenna shows several advantageous practical features, i.e., it is fed by a simple L-probe that covers both the N257 $(26.5 - 29.5$ GHz) and N258 $(24.25 - 27.5$ GHz) 5G mmWave frequency ranges. The integration of RFIC components, including the design of the beamformer transition, is explained in detail. In addition, the impact of the transition design on the performance of the IMED array antenna before and after its implementation is being investigated. The proposed IMEDs were manufactured and integrated with two distinct analogue beamformer RFICs (*MMW 9004 KC* and *MMW 9002 KC*) to produce the integrated MED (IMED) antenna and tested experimentally. The suggested IMED with the *MMW 9004 KC* demonstrates an EIRP at P1dB of 35.3 dBm at 26 GHz, whereas the IMED with *MMW 9004 KC* demonstrates an EIRP at P1dB of 35.1 dBm at 28 GHz. The performance of the measured IMEDs is in excellent agreement with simulations and theoretical computations. Based on the work presented, we conclude that it is feasible to develop a single wideband AiP that is easy to integrate with distinct analogue beamformers operating within the frequency band of the proposed antenna. This is possible provided the employed RFICs are designed and packaged with the same footprint for RF ports, SPI control ports, and DC power supply ports. In addition, the proposed IMED could be extended as the phased array antenna with beam scanning capability at both E- and H-planes. As demonstrated in our simulated result, the proposed MED could support the scanning up to $\pm 50°$ and $\pm 40°$, for the E- and H-planes, respectively, with a gain loss of ≤ 3 dB. Moreover, additional RF components such as Wilkinson power dividers, filters, and local oscillators can be introduced to the antenna's common RF input/output port, allowing the antenna system engineer to readily modify the AiP to the application needs and regional standards. Consequently, the suggested AiP is a promising candidate for mmWave 5G applications. Future work will concentrate on developing an AiP based on the MED design for a larger array, which could potentially be utilized in 5G outdoor base stations. Additionally, integrating other components such as diplexers, up and down-converters, and local oscillators into a single package will be a key area of focus. Furthermore, for a sustainable future, exploring additively manufactured AiP solutions for mmWave and sub-THz band applications will be of significant interest.

Data availability statement

The raw data supporting the conclusions of this article will be made available by the authors, without undue reservation.

Author contributions

AG: Funding acquisition, Methodology, Project administration, Resources, Supervision, Writing–review and editing. WY: Conceptualization, Data curation, Formal Analysis, Investigation, Methodology, Software, Validation, Visualization, Writing–original draft.

Funding

Acknowledgments

Conflict of interest

Author WY was employed by Rohde & Schwarz GmbH Co.KG.

The remaining author declares that the research was conducted in the absence of any commercial or financial relationships that could be construed as a potential conflict of interest.

The author(s) declared that they were an editorial board member of Frontiers, at the time of submission. This had no impact on the peer review process and the final decision.

Publisher's note

References

Alibakhshikenari, M., Virdee, B. S., Salekzamankhani, S, et al. (2021a). High-isolation antenna array using SIW and realized with a graphene layer for sub-terahertz wireless applications. *Scientific Reports* 11, 10218. doi:10.1038/s41598-021-87712-y

Alibakhshikenari, M, Virdee, B. S., Althuwayb, A. A., et al. (2021b). Study on on-chip antenna design based on metamaterial-inspired and substrate-integrated waveguide properties for millimetre-wave and thz integrated-circuit applications. *Journal of Infrared, Millimeter, and Terahertz Waves* 42, 17–28. doi:10.1007/s10762-020-00753-8

Alhamed, A., Gültepe, G., and Rebeiz, G. M. (2022). A multi-band 16–52-GHz transmit. *IEEE J. Solid-State Circuits* 57, 1280–1290. doi:10.1109/jssc.2021.3134325

Aoudia, M., Alaraj, M. B., Abu Waraga, O., Mokhamed, T., Abu Talib, M., Bettayeb, M., et al. (2024). Toward better blockchain-enabled energy trading between electric vehicles and smart grids in Internet of Things environments: a survey. *Frontiers in Energy Research* 12, 1393084. doi:10.3389/fenrg.2024.1393084

Burasa, P., Djerafi, T., and Wu, K. (2021). A 28 GHz and 60 GHz dual-band on-chip antenna for 5G-compatible IoT-served sensors in standard CMOS process. *IEEE Trans. Antennas Propag.* 69, 2940–2945. doi:10.1109/tap.2020.3025236

Chou, H. T., Chou, S. J., Deng, J. D., Chang, C. H., and Yan, Z. D. (2022). LTCC-based antenna-in-package array for 5G user equipment with dual-polarized Endfire radiations at millimeter-wave frequencies. *IEEE Trans. Antennas Propag.* 70, 3076–3081. doi:10.1109/tap.2021.3118819

Da Costa Nascimento, J. J., Marques, A. G., Adelino Rodrigues, Y. O., et al. (2024). Health of Things Melanoma Detection System—detection and segmentation of melanoma in dermoscopic images applied to edge computing using deep learning and fine-tuning models. *Frontiers in Communications and Networks* 5, 1376191. doi:10.3389/frcmn.2024.1376191

ETSI (2013). Machine-to-Machine communications (M2M); Functional architecture. *Tech. Rep. ETSI TS.*

GSMA Intelligence (2021). The Economics of mmWave 5G - an assessment of total cost of ownership in the period to 2025. *Tech. Rep. Qualcomm Technol.*

Gu, X., Liu, D., Baks, C., Tageman, O., Sadhu, B., Hallin, J., et al. (2019). Development, implementation, and characterization of a 64-element dual-polarized phased-array antenna module for 28-GHz high-speed data communications. *IEEE Trans. Microw. Theory Tech.* 67, 2975–2984. doi:10.1109/tmtt.2019.2912819

Gu, X., Liu, D., Hasegawa, Y., Masuko, K., Baks, C., Suto, Y., et al. (2021). Antenna-in-package integration for a wideband scalable 5G millimeter-wave phased-array module. *IEEE Microw. Wirel. Components Lett.* 31, 682–684. doi:10.1109/lmwc.2021.3071917

Hansen, R. C. (2009). *Phased array antennas.* John Wiley & Sons.

Hwang, I. J., Ahn, B., Chae, S. C., Yu, J. W., and Lee, W. W. (2019). Quasi-Yagi antenna array with modified folded dipole driver for mmWave 5G cellular devices. *IEEE Antennas Wirel. Propag. Lett.* 18, 971–975. doi:10.1109/lawp.2019.2906775

Jang, T. H., Jung, K. P., and Park, C. S. (2023). Broadband millimeter-wave antenna in package with L-probed E-shaped patch covering 57 GHz to 71 GHz. *IEEE Trans. Antennas Propag.* 71, 89–98. doi:10.1109/tap.2022.3215225

Kibaroglu, K., Sayginer, M., and Rebeiz, G. M. (2018). A low-cost scalable 32-element 28-GHz phased array Transceiver for 5G communication Links based on a 2 × 2 beamformer Flip-chip Unit cell. *IEEE J. Solid-State Circuits* 53, 1260–1274. doi:10.1109/jssc.2018.2791481

Kildal, P. S. (2015). *Foundations of antenna engineering: a unified approach for line-of-sight and multipath.* London, United Kingdom and Boston, United StatesArtech House.

Kim, D., Hirokawa, J., Ando, M., Takeuchi, J., and Hirata, A. (2014). 64 × 64-Element and 32 × 32-element slot array antennas using Double-layer Hollow-waveguide Corporate-feed in the 120 GHz band. *IEEE Trans. Antennas Propag.* 62, 1507–1512. doi:10.1109/TAP.2013.2296318

Kumar, M., and Chand, S. (2020). A secure and efficient cloud-centric internet-of-medical-things-enabled smart healthcare system with public verifiability. *IEEE Internet Things J.* 7, 10650–10659. doi:10.1109/jiot.2020.3006523

Kuo, H. C., Kuo, C. W., Wang, C. C., and Hung, C. P. (2022). A D-band magneto-electric dipole antenna-in-package (AiP) implemented on BT-based organic substrate. *IEEE Trans. Components, Packag. Manuf. Technol.* 12, 1673–1680. doi:10.1109/tcpmt.2022.3211500

Li, M., and Luk, K. M. (2015). Wideband magneto-electric dipole antenna for 60-GHz millimeter-wave communications. *IEEE Trans. Antennas Propag.* 63, 3276–3279. doi:10.1109/tap.2015.2425418

Liao, Y., de Freitas Rocha Loures, E., and Deschamps, F. (2018). Industrial Internet of Things: a systematic literature review and insights. *IEEE Internet Things J.* 5, 4515–4525. doi:10.1109/jiot.2018.2834151

Luk, K. M., and Wong, H. (2006). A new wideband unidirectional antenna element. *Int. J. Microw. Opt. Technol.* 1, 35–44.

Mak, C. L., Luk, K., Lee, K., and Chow, Y. (2000). Experimental study of a microstrip patch antenna with an L-shaped probe. *IEEE Transactions on antennas and propagation* 48, 777–783. doi:10.1109/8.855497

Mehmood, Y., Haider, N., Imran, M., Timm-Giel, A., and Guizani, M. (2017). M2M communications in 5G: state-of-the-art architecture, recent advances, and

research challenges. *IEEE Commun. Mag.* 55, 194–201. doi:10.1109/mcom.2017.1600559

Minovski, D., Åhlund, C., and Mitra, K. (2020). Modeling quality of IoT experience in autonomous vehicles. *IEEE Internet Things J.* 7, 3833–3849. doi:10.1109/jiot.2020.2975418

Pozar, D. M. (2011). *Microwave engineering*. New Jersey, United States: John Wiley & Sons.

Rangan, S., Rappaport, T. S., and Erkip, E. (2014). Millimeter-wave cellular wireless networks: Potentials and challenges. *Proc. IEEE* 102, 366–385. doi:10.1109/jproc.2014.2299397

SalarRahimi, M., Vilela Pinto dos Anjos, E., Taghikhani, P., Volski, V., Fager, C., Schreurs, D. M. M. P., et al. (2020). A cost-efficient 28 GHz integrated antenna array with full impedance matrix characterization for 5G NR. *IEEE Antennas Wirel. Propag. Lett.* 19, 666–670. doi:10.1109/lawp.2020.2976188

Theis, G., Song, Z., Federico, G., Caratelli, D., and Smolders, A. B. (2021). A design framework for beamforming integrated circuits operating at mm-wave frequencies. *IEEE Access* 9, 62232–62240. doi:10.1109/access.2021.3073987

Wagih, M., Hilton, G. S., Weddell, A. S., and Beeby, S. (2022). Millimeter-wave power transmission for compact and large-area Wearable IoT devices based on a higher Order mode Wearable antenna. *IEEE Internet Things J.* 9, 5229–5239. doi:10.1109/jiot.2021.3107594

Wollschlaeger, M., Sauter, T., and Jasperneite, J. (2017). The future of industrial communication: Automation networks in the era of the internet of things and industry 4.0. *IEEE Ind. Electron. Mag.* 11, 17–27. doi:10.1109/mie.2017.2649104

Wu, K., Cheng, Y. J., Djerafi, T., and Hong, W. (2012). Substrate-integrated millimeter-wave and terahertz antenna technology. *Proc. IEEE* 100, 2219–2232. doi:10.1109/jproc.2012.2190252

Yin, Y., Zihir, S., Kanar, T., Ma, Q., Chung, H., Gao, L., et al. (2020). A 37-42-GHz 8x8 phased-array with 48-51-dBm EIRP, 64-QAM 30-Gb/s data rates, and EVM Analysis versus channel RMS errors. *IEEE Trans. Microw. Theory Tech.* 68, 4753–4764. doi:10.1109/tmtt.2020.2998183

Yong, W. Y., Hadaddi, A., and Glazunov, A. A. (2023). Design and characterization of the fully metallic gap waveguide-based frequency selective radome for millimeter wave fixed beam array antenna. *IEEE Trans. Antennas Propag.* 71, 531–541. doi:10.1109/tap.2022.3215454

Yong, W. Y., Haddadi, A., Emanuelsson, T., and Glazunov, A. A. (2020). A bandwidth-enhanced cavity-backed slot array antenna for mmwave fixed-beam applications. *IEEE Antennas Wirel. Propag. Lett.* 19, 1924–1928. doi:10.1109/lawp.2020.3022988

Zhai, H, Zhang, J, Zang, Y, Gao, Q, and Liang, C (2014). An LTE base-station magnetoelectric dipole antenna with anti interference characteristics and its MIMO system application. *IEEE Antennas and Wireless Propagation Letters* 14, 906–909. doi:10.1109/LAWP.2014.2384519